J Solid State Electrochem (2000) 4: 367–382

REVIEW

Venkat Srinivasan · John W. Weidner · Ralph E. White

Mathematical models of the nickel hydroxide active material

Received: 17 October 1999 / Accepted: 26 December 1999

Abstract A review is presented of the mathematical models that have been developed to describe the phenomena that occur in the active material in the nickel electrode. The review includes models that describe the reaction thermodynamics, proton diffusion, electron conductivity, semiconductor effects, and the reactions in the solid phase. The appropriateness of these models and their usefulness in predicting phenomena observed in nickel-based batteries are discussed.

Key words Nickel hydroxide · Battery · Mathematical model · Diffusion · Electronic conductivity

Introduction

The nickel electrode has been used for years in a number of systems, including the nickel-cadmium, nickel-metal hydride, nickel-zinc, and nickel-hydrogen batteries [1]. However, even after a century of research and development, this electrode is still not understood completely. This is due to the complex nature of the nickel hydroxide/oxyhydroxide behavior and the close relationship between the structure of the material and its electrochemical characteristics [2]. In this paper, we review the efforts that have been undertaken to model the nickel hydroxide active material over the last two decades. The purpose of the review is twofold: (1) to give the reader an understanding of the theoretical basis for the various chemical and electrochemical phenomena observed in the nickel electrode and (2) to detail the efforts in developing design tools that relate various active material characteristics (e.g., diffusion, conductivity) to the performance.

Figure 1 presents a schematic of a cross section of a cell constructed with a nickel positive electrode. The negative electrode used in the cell could be a porous cadmium, metal hydride, zinc, or gas-fed hydrogen electrode. The nickel hydroxide/oxyhydroxide active material is supported on a conductive sinter of nickel metal (substrate) with the active material either pasted or impregnated into the pores of the sinter. There is considerable void volume in the electrode, which is flooded with electrolyte, typically concentrated KOH at 30% (by weight) [3]. The main chemical and electrochemical reactions that occur at the nickel electrode can be ideally represented as [4]:

$$H^+ + OH^- \underset{\text{discharge}}{\overset{\text{charge}}{\rightleftharpoons}} H_2O \quad (1)$$

$$Ni(OH)_2 \underset{\text{discharge}}{\overset{\text{charge}}{\rightleftharpoons}} NiOOH + H^+ + e^- \quad (2)$$

These reactions on charge are represented schematically in Fig. 1. A proton and an electron are released at the reaction site on the active material, after which the electron travels to the conducting substrate (typically nickel metal) and eventually out to the external circuit. The proton diffuses through the active material to the solid/electrolyte interface, where it combines with a hydroxyl ion to form water. On discharge, these processes are reversed.

In order to predict the performance of the nickel electrode over a wide range of designs and operating conditions, a number of processes must be accounted for in terms of measurable parameters, namely: (1) thermodynamics and kinetics of all redox reactions; (2) transport of ions through all ionically conducting phases; and (3) the potential variations in both ionically and electronically conducting phases. The high concentration of OH^- in the cell necessitates the use of concentrated solution theory [5–9], where the interactions of the ions with one another and the solvent (water) need to

V. Srinivasan · J.W. Weidner · R.E. White (✉)
Department of Chemical Engineering,
Swearingen Engineering Building,
University of South Carolina, Columbia, SC 29208, USA
e-mail: white@engr.sc.edu
Tel.: +1-803-7773270; Fax: +1-803-7778265

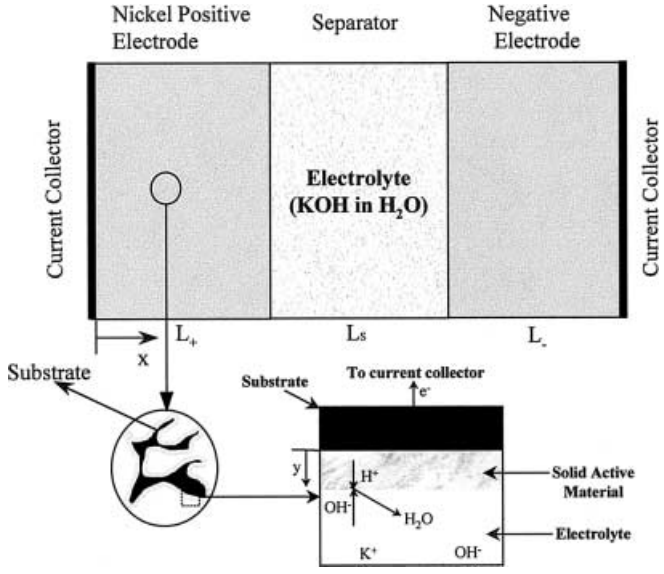

Fig. 1 Schematic of a cell with a nickel positive electrode, separator, and a negative electrode. The negative electrode could be a porous cadmium, metal-hydride, etc., or gas-fed hydrogen electrode. The reactions occurring in the positive electrode on charge are shown

be considered. The complications introduced by the presence of the porous matrix are handled by using porous electrode theory [8, 10–12].

Macroscopic, porous electrode models have been developed for nickel batteries [13–27] in order to understand how the complex interactions that occur among the anode, cathode, and separator affect battery performance. For example, Micka and Rousar [13, 14] developed a one-dimensional model for the nickel electrode, but they noticed that on discharge the voltage curves could not be fitted adequately by assuming an ideal solution for the solid phase. Fan and White [17] improved the predictions of the discharge curves by using activity-coefficient corrections to the equilibrium potential, as suggested by Barnard et al. [28]. However, their model was unable to predict adequately the percent utilization of the active material on discharge as a function of current. Mao et al. [27] improved predictions of utilization by adding the diffusional resistance of protons to their pseudo two-dimensional model. However, this model was unable to predict the change in performance of the battery on cycling because the redox reaction in the active material was assumed to be the overly simplistic Eq. (2). Adding a more sophisticated reaction mechanism to the model is required in order to predict performance during cycling.

As the above examples illustrate, the limitations of previous nickel battery models have been due to the limited understanding of how the nickel hydroxide active material behaves. As improvements have been made in predicting the behavior of the active material, the predictions of the battery models have improved. Therefore, this review will concentrate on models that have been developed to predict various phenomena that occur in the nickel hydroxide active material. The review will include models that describe (1) the equilibrium potential [26, 28–30], (2) proton diffusion [18, 31–40], (3) electronic conductivity and semiconductor effects [27, 35, 41, 42], and (4) reactions in the solid phase [25, 43]. Ultimately, the information that is gained from models of the active material need to be incorporated into models that couple variations in the microscopic active material with variations in the macroscopic porous electrodes. See references [19–27] for this pseudo two-dimensional approach.

Modeling of the active material

Equilibrium potential

Developing thermodynamic models for the nickel electrode that predict the equilibrium potential as a function of state-of-charge are complicated by three issues: (1) O_2 evolution that occurs along with the nickel reaction according to

$$4OH^- \rightarrow O_2 + 2H_2O + 4e^- \tag{3}$$

(hence the potential observed is a mixed potential [44]); (2) a hysteresis between charge and discharge that results in a 50–90 mV offset between the two processes [3]; and (3) a nickel reaction that is more complex than that shown by reactions (1) and (2). Nonetheless, investigators have attempted to measure the equilibrium potential as a function of state-of-charge (SOC). One approach is to perform discharge experiments at rates that are low enough that kinetic and mass transfer resistances are negligible, but high enough that oxygen evolution is not appreciable. These low-rate discharge curves are distinguished by two main features: (1) the potential is relatively independent of the SOC at intermediate states of charge; and (2) the curve is asymmetric with a gradual decrease in voltage with decreasing SOC at high states of charge, and a sharp drop in voltage at low states of charge. By assuming the material consists of pairs of coexisting solid solutions, the equilibrium potential of the material can be expressed in terms of the activity of the species (hydroxide and oxyhydroxide) using the Nernst equation:

$$E = E^\circ + \frac{RT}{F}\ln\left(\frac{a_{\mathrm{Ni(OH)_2}}}{a_{\mathrm{NiOOH}}}\right) \tag{4}$$

Considerable variations in the equilibrium potential profiles can be achieved based on the change in activity. For example, by assuming the activity coefficients are equal to 1.0, the activities in Eq. (4) can be replaced by the concentration of the oxidized and reduced species [13, 14]. However, the resulting expression does not capture the two essential features of a low-rate discharge curve as described above. Barnard and co-workers [28] studied the reversible potential of the reaction by incorporating non-idealities into the equilibrium expression. They used a one-parameter Margules expression to

rewrite Eq. (4) in terms of the SOC of the active material, θ, which results in the following expression:

$$E = E^{\circ} + \frac{RT}{F}\ln\left(\frac{\theta}{1-\theta}\right) + \frac{RT}{F}A(1-2\theta) \tag{5}$$

Other one-parameter activity models result in expressions similar to Eq. (5) [28, 29]. The one-parameter models are considered valid if the intercalation process occurs randomly (i.e., all intercalation sites are of equivalent energy) [45]. The effect of the intercalation constant is to flatten the potential in the middle of the discharge, as shown by Barnard [28], Fan and White [17], and Jain et al. [29]. However, the curve remains symmetric about the mid point (50% SOC), similar to Eq. (4).

The asymmetry (i.e., a gradual decrease in voltage at high states of charge and a sharp drop at low states of charge) can be incorporated by using two-parameter activity coefficient models [28, 29], which suggest that the insertion of protons into the lattice occurs in an ordered, non-random fashion [45]. For example, the two-parameter Margules equation results in the following form of the equilibrium potential as a function of θ:

$$E = E^{\circ} + \frac{RT}{F}\ln\left(\frac{\theta}{1-\theta}\right) + \frac{RT}{2F}\Big[-2A_0 + 4A_0(1-\theta) - 2B_0 + 6B_0(1-\theta) - 3B_0(1-\theta)^2\Big] \tag{6}$$

Jain et al. [29] compared this and other models to experimental data on thin films of nickel hydroxide with 12% cobalt additive. They extracted the activity coefficient parameters and the equilibrium potential as a function of temperature.

Paxton and Newman [26] did not start with an activity-coefficient model to obtain E as a function of θ. Rather, they fit an empirical model to experimental data measured by Conway and Gileadi [46] to obtain the following relationship:

$$\left.\begin{aligned} E &= E^{\circ} + \frac{RT}{F}\ln\left(\frac{\theta}{1-\theta}\right) \quad \text{for } \theta \geq 0.0545 \\ E &= E^{\circ} - 0.052335 - 0.054284\ \exp[-18.652\theta] \\ &\quad - 0.37142\ \exp[-104.15\theta] \end{aligned}\right\} \quad \text{for } 0.0545 \geq \theta \geq 0 \tag{7}$$

Figure 2 shows the equilibrium potential curves obtained by plotting $(E - E^{\circ})$ using Eqs. (4)–(7). The solid line represents an ideal solid solution generated using Eq. (5) for $A = 0$. Both the one-parameter and the two-parameter models shown in Fig. 2 were generated using the intercalation constants estimated by Jain et al. [29] for nickel hydroxide films with 12% cobalt additive, at 27 °C. Using a one-parameter fit flattens the voltage profile through most of the discharge. In addition, the sharp drop in potential at low and high states of charge is attenuated. The curves can be made asymmetric with a gradual drop at low states of charge and a sharp drop at high states of charge by using a two-parameter model.

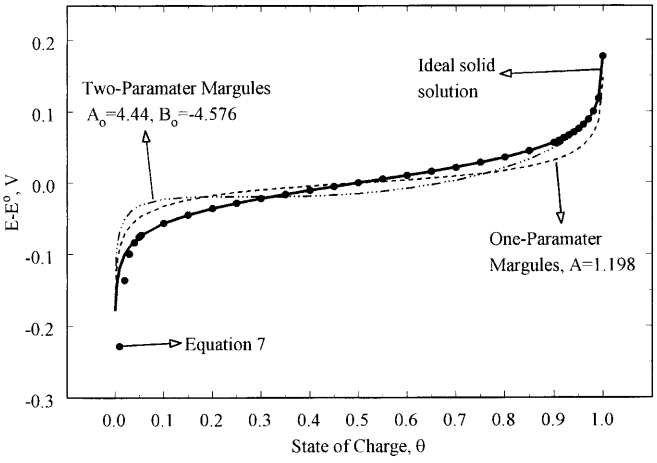

Fig. 2 Equilibrium potential of the nickel hydroxide electrode as a function of the state-of-charge: (——) denotes the curve generated for an ideal solid solution, (- - - - -) denotes the one-parameter Margules (Eq. 5) and (-·-·-·) the two-parameter Margules expression (Eq. 6). The symbol (•) denotes the curve generated using Eq. (7)

Figure 2 also shows the curve obtained by plotting Eq. (7) (symbols). As expected, the curve follows the ideal case through most states of charge. However, at low states of charge (below 0.0545) the second part of Eq. (7) is used, which makes the drop in potential sharper than at high states of charge.

While the above investigations have assumed the discharge curve to be representative of the true equilibrium, Ta and Newman [30, 47] modeled the hysteresis effect by considering the equilibrium to be at the mid-point between charge and discharge. The authors [30, 47] used experimental data to obtain the following empirical fit for E versus θ:

$$E = E^{\circ} + 0.04\ \exp[45(\theta-1)] - 0.5\ \exp[-55\theta] - 0.012\ln\left[\frac{(1-\theta)}{\theta}\right] \pm \begin{cases} 0.046 & \text{for pure Ni(OH)}_2 \\ 0.025 & \text{for Co-doped Ni(OH)}_2 \end{cases} \tag{8}$$

The $\pm$ term is positive on charge and negative on discharge. Figure 3 sketches $(E - E^{\circ})$ obtained using Eq. (8), for both the pure $Ni(OH)_2$ and cobalt-doped electrodes. The hysteresis between the two loops is clear in the figure, as is the lower hysteresis on the cobalt-doped electrode. The graph also shows the potential for an ideal solid solution for comparison. A physical explanation for the hysteresis shown in Fig. 3 is lacking. The only cell model to consider this effect was reported recently by Timmerman and co-workers [25], where a exponential expression was used, the basis of which was assumed to be the Schottky barrier that is speculated to form between the metal substrate and the semiconducting oxide. This Schottky barrier acts as a rectifying contact during charge, hence resulting in an increase in the potential. On the other hand, the drop is

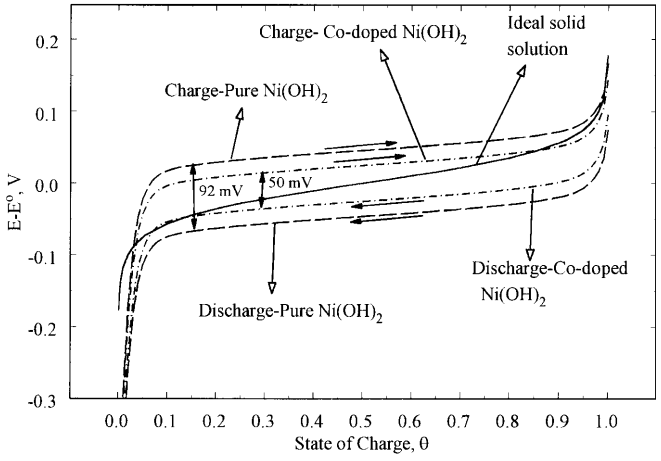

Fig. 3 Equilibrium potential of the nickel hydroxide electrode as a function of the sate-of-charge on charge and discharge for pure $Ni(OH)_2$ and Co-doped $Ni(OH)_2$ electrodes. The curves were generated using Eq. (8). The ideal solid solution is also shown for comparison

negligible on the discharge. However, the recent evidence by Ta and Newman suggests that the effect is more likely to be a hysteresis that arises due to some differences in the mechanism between the charge and discharge [38, 47]. More experiments are needed in order to understand this phenomenon better.

Proton diffusion

Figure 1 shows the active material impregnated into the pores of the nickel sinter. Although there is speculation as to whether the active material is itself porous, most of the modeling efforts until this date have considered the active material to be a non-porous electrode of either planar [19, 24, 25], cylindrical [20–23, 27], or spherical [26] geometry. The reactions taking place in the active material during charge are shown in the figure. The charge/discharge reaction is assumed to occur at the film/electrolyte interface (owing to the non-porous active material assumption) according to reaction (2). Proton diffusion into the bulk of the active material makes it possible for this reaction to continue at the interface. Models of proton diffusion into the nickel hydroxide active material have been used both as a means of understanding how proton diffusion affects electrochemical performance [35, 39, 40], and as a means of estimating the diffusion coefficient [18, 31–34, 36–38]. These studies modeled one of four electrochemical experiments: (1) cyclic voltammetry [31, 32, 38], (2) potential step [18, 32–34, 38], (3) electrochemical impedance spectroscopy [36, 37], and (4) constant-current charge/discharge curves [35, 39, 40]. We start the section by discussing proton diffusion and the efforts at obtaining the diffusion coefficient, and then review models that were developed to understand its effect on constant-current charge and discharge.

Diffusion coefficient estimation

Early attempts to evaluate the proton diffusion coefficient were based on cyclic voltammetry [31, 32] and potential step [18, 32–34] experiments. However, the values measured vary by three orders of magnitude from 1×10^{-9} to $1 \times 10^{-12}\,cm^2/s$. Models that predict the constant-current discharge of the cell show that the value used is critical in predicting the utilization at high discharge rates. For example, Mao et al. [27] showed that while using a value of $1 \times 10^{-10}\,cm^2/s$ ensured complete utilization for a 10 C discharge, using $1 \times 10^{-12}\,cm^2/s$ resulted in an 80% loss in utilization. In addition, Lukovtsev and Slaidin [48] reported that the diffusion coefficient of protons increases with increase in the SOC of the electrode. However, no data were reported and their analysis was purely qualitative. Clarification of the ambiguity in the measured values necessitated the development of more robust techniques, two of which are discussion below.

Motupally et al. [36, 37] used electrochemical impedance spectroscopy (EIS) to measure the diffusion coefficient of protons on a thin film of nickel hydroxide with 12% cobalt additive deposited on a gold substrate. The mass of the film was measured using an electrochemical quartz crystal microbalance (EQCM), from which the authors deduced a thickness of 1–1.5 μm, based on a density of $3.5\,g/cm^3$ [49]. After the deposition, the films were cycled in 3% KOH and discharged to a known SOC and an EIS experiment conducted. The Nyquist plots showed a semicircle at high frequencies, attributed to the combined effect of the nickel oxidation reaction and double layer charging, and a 45° line at moderate frequencies transitioning to a slope of ∞ at low frequencies. The slope of the Nyquist plot in the transition was used to find the diffusion coefficient.

In order to analyze the data and extract a diffusion coefficient, the authors developed an impedance model based on Fick's diffusion equation:

$$\frac{\partial c_{H^+}}{\partial t} = D_{H^+}\frac{\partial^2 c_{H^+}}{\partial y^2} \tag{9}$$

with the boundary conditions

$$\begin{aligned} &@t = 0 \quad c_{H^+} = c^{\circ}_{H^+} \\ &@y = 0 \quad \frac{\partial c_{H^+}}{\partial y} = 0 \\ &@y = \delta \quad D_{H^+}\frac{\partial c_{H^+}}{\partial y} = \frac{I}{F} \end{aligned} \tag{10}$$

The authors converted Eq. (9) to an ordinary differential equation using Laplace transforms and solved the equation with the boundary conditions given in Eq. (10). They then converted the resulting equation to the frequency domain and obtained expressions for the impedance of the system as a function of frequency. Analogous procedures have been used by Land and Inzelt [50], Tribollet and Newman [51], Fuller [52], and

Viner and Fedkiw [53], for evaluating the impedance of other electrochemical systems. Note that Eq. (9) assumes that the diffusion coefficient is independent of the SOC (i.e., proton concentration) – an assumption considered valid in an impedance experiment, as the voltage perturbation (~5 mV) is small enough not to cause appreciable change in the SOC.

Motupally et al. [36, 37] evaluated the slope of the imaginary vs. real component from their equations and equated it to the experimental data in the transition region (transition from 45° to slope of ∞) to estimate the diffusion coefficient as a function of SOC. The authors found that the diffusion coefficient data changed as a function of SOC and followed the trend given by:

$$D_{H^+} = D_{NiOOH}\left[\theta + (1-\theta)\left(\frac{D_{Ni(OH)_2}}{D_{NiOOH}}\right)^{1/2}\right]^2 \tag{11}$$

with $D_{Ni(OH)_2} = 6.4 \times 10^{-11}\,cm^2/s$ and $D_{NiOOH} = 3.4 \times 10^{-8}\,cm^2/s$. Equation (11) is a mixing rule in terms of the root mean square displacement of the diffusing species in a solid solution comprising a homogeneous mixture of two phases [37]. This functionality was proposed by Bouet et al. [19] and used in their pseudo two-dimensional model. Motupally et al. [36, 37] were also able to ascertain that the change they observed with SOC was that of the diffusion coefficient and not due to change in the diffusional length (e.g., a moving reaction front). They argued that a moving front would not result in the functional form for the diffusion coefficient as a function of SOC given by Eq. (11). The authors explain the sharp drop in diffusion coefficient at low states of charge by speculating that the proton diffusion occurs by a hopping mechanism where the proton hops from one oxyhydroxide site to another. As the SOC decreases, the concentration of NiOOH decreases, and hence the diffusion coefficient decreases. However, the authors caution that the impedance technique cannot differentiate between diffusion limitations caused by protons and those due to mixed conduction involving protons and electrons.

MacArthur [33], Briggs and Snodin [34], Fan [18], and recently Ta and Newman [38] measured the diffusion coefficient of protons in nickel hydroxide films using a potential step experiment. Following a potential step, the diffusion equation, (Eq. 9) can be solved for a finite slab with the initial and boundary conditions:

$$\begin{aligned} &@t = 0 \quad c_{H^+} = c^{\circ}_{H^+} \\ &@y = 0 \quad \frac{\partial c_{H^+}}{\partial y} = 0 \\ &@y = \delta \quad c_{H^+} = c_{eq} \end{aligned} \tag{12}$$

which leads to an expression of the form [32–34]:

$$I(t) = \frac{2D_{H^+}(c_{eq} - c^{\circ}_{H^+})}{\delta}\sum_{n=0}^{\infty}\exp\left(-\frac{D_{H^+}(2n+1)^2\pi^2 t}{4\delta^2}\right) \tag{13}$$

The boundary condition at $y = \delta$ assumes that there is negligible charge-transfer resistance (i.e., the surface concentration equilibrates instantly to the new potential). MacArthur [33] minimized the effect of this assumption by using large potential steps (150–250 mV), which forces the surface concentration of protons to zero. By assuming that at long times the term with $n = 0$ is the only significant term, MacArthur showed a method for extracting δ from the experimental data. Using cathodically precipitated films of thickness ~1 μm, he estimated a diffusion coefficient of $5–7 \times 10^{-11}\,cm^2/s$ during discharge and $3–5 \times 10^{-10}\,cm^2/s$ on charge. However, the authors note that there is considerable qualitative difference in the current-time plots on charge and discharge. One reason for this asymmetry may be that a large potential step results in a large change in oxidation state during the experiment. If D_{H^+} changes with oxidation state, Eq. (13) is no longer valid and a positive potential step would be different from a negative one.

A convenient approximation can be made to the potential-step analysis at short times by replacing the boundary condition at $y = \delta$ with:

$$@y \to \infty \quad c_{H^+} = c^{\circ}_{H^+} \tag{14}$$

The solution to this semi-infinite model is the Cottrell equation [32, 34, 54]:

$$I(t) = \frac{D^{1/2}_{H^+}F(c_{eq} - c^{\circ}_{H^+})}{\pi^{1/2}t^{1/2}} \tag{15}$$

Both the short-term and long-term solutions were used by Briggs and Snodin [34] in their analysis. They used potential steps of ~10–20 mV negative of the discharge curves on thin films of pure nickel hydroxide (~0.4–2 μm) deposited using cathodic precipitation. They estimated diffusion coefficients of $\sim 4 \times 10^{-13}\,cm^2/s$ for γ-NiOOH and $1 \times 10^{-12}\,cm^2/s$ for β-NiOOH. The authors further confirmed that the short-time assumption was valid by using the diffusion coefficient estimated using Eq. (15) in Eq. (13), which yielded adequate fits. Subsequently, Zhang and Park [32] used both these methods and estimated a diffusion coefficient of $5 \times 10^{-12}\,cm^2/s$. They used anodically formed films of thickness 10 nm, and potential steps of the order of 1.2 V.

Although some of the experimental data collected by Briggs and Snodin [34] and Zhang and Park [32] showed a linear $I(t)$ vs. $1/\sqrt{t}$ as predicted by Eq. (15), not all their data did. Using potential steps of 5 mV on ~1 μm thick Ni-Co films, Fan [18] also observed that the data were not consistent with either Eq. (13) or Eq. (15). He assumed that the cause for the discrepancy was the assumption of a fast reaction rate at the surface of the film. Therefore, he substituted the concentration boundary condition at $y = \delta$ with a linearized Butler-Volmer equation. The author solved the equation analytically and used a least squares fitting technique to estimate the diffusion coefficient and two kinetic

constants. This technique yielded diffusion coefficients on the order of $2–5 \times 10^{-8}\,cm^2/s$, consistent with the results of Motupally et al. [36, 37].

Ta and Newman [38] developed a model that included proton diffusion, charge-transfer resistance, and oxygen evolution, and used it to simulate constant-current discharges, cyclic voltammograms, and current transients due to a potential step. In order to estimate the diffusion coefficient, a simulated potential step was fit to experiment data collected on cathodically deposited films of nickel hydroxide with cobalt additives and thicknesses of ~20–40 nm. Large potential steps were used (~170–300 mV), which meant that the SOC of the material was changing considerably during the experiment. Although their model assumed a priori that the diffusion coefficient did not change during the experiment (i.e., it was assumed independent of the SOC), they obtained values that increased with an increase in the SOC. Although this qualitative trend is consistent with the results of Motupally et al. [36, 37], the values they measured ($\sim 1 \times 10^{-12}\,cm^2/s$ at 50% SOC) are approximately three to four order of magnitude lower than the values reported by Motupally et al. (e.g., $\sim 1 \times 10^{-8}\,cm^2/s$ at 50% SOC) and consistent with that of Briggs and Snodin [34] and Zhang and Park [32].

Figure 4 summarizes the diffusion coefficient measurement reported in the literature. The reported values range from $2 \times 10^{-13}\,cm^2/s$ [30, 38] to $4 \times 10^{-8}\,cm^2/s$ [18]. While the measurements of Motupally et al. [37] and Ta and Newman [38] were a function of SOC, the rest of the authors were not and are represented by horizontal lines. Equation (11) was used to represent the values reported by Motupally et al. [37], while those of Ta and Newman [38] are indicated by the shaded region.

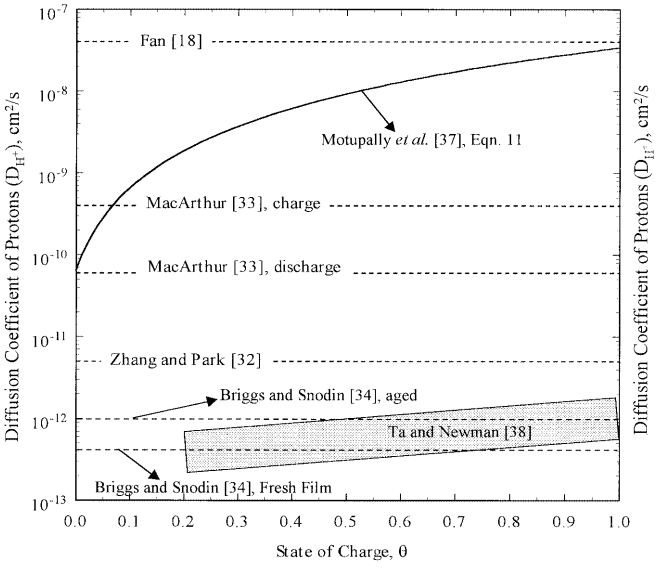

Fig. 4 Diffusion coefficient of protons in the nickel hydroxide electrode as a function of the state-of-charge as reported in the literature. While the measurements of Ta and Newman [38] and Motupally et al. [37] were reported as a function of state-of-charge, the rest were not, and hence are represented by *horizontal lines*

While the investigations reported above consider the movement of protons through the film to be a diffusion-controlled process, Yoon and Pyun [55] consider diffusion of hydrogen through the film in the presence of hydrogen traps. The authors show the effect of the trap density, capture rate, and release rate on current transients after a potential step. The authors then perform experiments on thin films of nickel hydroxide with different cobalt content with potential steps of 150–400 mV. Comparing the model with experimental data, Yoon and Pyun estimate the velocity and mobility of the phase boundary and conclude that incorporation of cobalt increases the velocity of the phase boundary. No estimate of proton diffusion coefficient was made in this study.

Models to describe diffusion in the active material

A qualitative understanding of the effect of charge-transfer resistance, proton diffusion, and electron conductivity during constant-current discharge was provided by Weidner and Timmerman [35]. They modeled the active material as a non-porous planar film, with the reaction occurring at the film electrolyte interface. The authors solved the equations for a constant-diffusion coefficient and neglected the oxygen evolution reaction. The latter assumption was considered valid since only discharge behavior was being studied. With these approximations, the governing equation and boundary conditions reduce to Eqs. (9) and (10). The solution to this equation is the following integral expression:

$$\frac{c_{H^+}}{c^{\circ}_{H^+}} = 1 - \frac{\delta}{F c_{H^+,max} D_{H^+}(1-\theta^{\circ})} \int_0^t \left\{ 1 + 2\sum_{k=1}^{\infty}(-1)^k \times \exp\left[-k^2\pi^2\left(\frac{D_{H^+}}{\delta^2}(t-z)\right)\right] \times \cos\left(k\pi\frac{y}{\delta}\right)\right\} I(z)\,dz \qquad (16)$$

Equation (16) can be integrated directly if the current density is known (e.g., constant-current discharge) or numerically if the current is unknown (e.g., potential control or when the reaction distribution in the porous electrode is not uniform).

The integrated form of Eq. (16) was coupled to a Butler-Volmer kinetic expression and Ohm's law for the solid phase to obtain the voltage as a function of SOC (i.e., discharge curves). The effect of charge-transfer resistance, proton diffusion, and electron conductivity on the discharge curves were studied separately. In the case of charge-transfer resistance, an increase in this resistance resulted in a lower mid-voltage plateau and reduced curvature at the start of discharge, as shown in Fig. 5. In this figure the voltage is plotted as a function of the state-of-discharge $(1-\theta)$ for different values of I_0, defined by the authors as:

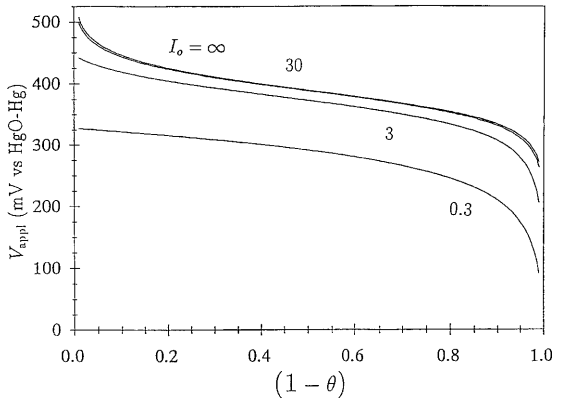

Fig. 5 Effect of charge transfer resistance on nickel hydroxide discharge curves. As I_0 (defined in Eq. 17) decreases, the charge transfer resistance increases (reproduced from [35] by permission of The Electrochemical Society)

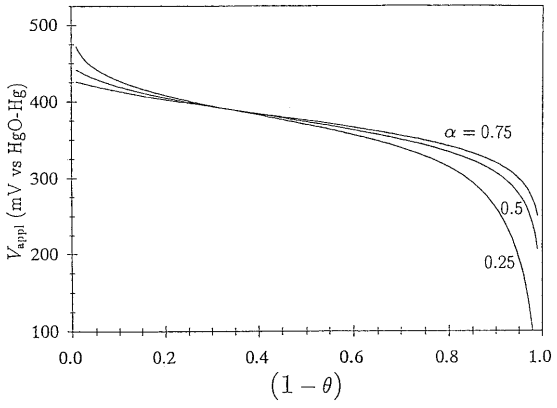

Fig. 6 Effect of the transfer coefficient, α, on nickel hydroxide discharge curves. The discharge curves are only affected by α when charge transfer resistance is appreciable (reproduced from [35] by permission of The Electrochemical Society

$$I_0 = \frac{t_d i_{0,ref}}{F c_{H^+,max} \delta} \equiv \frac{\text{discharge time}}{\text{charge-transfer resistance}} \tag{17}$$

The authors [35] also studied the effect of the transfer coefficient, α, and concluded that decreasing α increases the S-shape of the discharge curve, as seen in Fig. 6. In addition, the sensitivity of the discharge curve to α increases as I_0 decreases. Finally, very little decrease in utilization is seen owing to changes in these two kinetic parameters.

In contrast to kinetic resistance, a decrease in utilization can be seen when the mass transfer resistance is increased, as shown in Fig. 7. In this figure the voltage is plotted as a function of the state-of-discharge for different values of $\mathscr{D}$ defined as

$$\mathscr{D} = \frac{t_d D_{H^+}}{\delta^2} \equiv \frac{\text{discharge time}}{\text{diffusion resistance}} \tag{18}$$

Based on their qualitative results, the authors concluded that the important factors needed to predict nickel hydroxide discharge curves are: (1) diffusion coefficient of protons; (2) thickness of the hydroxide film; (3) initial SOC; and (4) electronic conductivity (see section below) as a function of SOC at the end of discharge.

While Weidner and Timmerman [35] modeled the nickel hydroxide film with a constant diffusion coefficient, Motupally et al. [39] included the SOC dependence to model the same system. This change modifies the diffusion equation to the form:

$$\frac{\partial c_{H^+}}{\partial t} = \frac{\partial}{\partial y}\left(D_{H^+} \frac{\partial c_{H^+}}{\partial y}\right) \tag{19}$$

with the boundary and initial conditions given in Eq. (10). By numerically solving Eq. (19) coupled with Eq. (11), Motupally et al. compared the utilization as a function of current when the diffusion coefficient was constant and variable. They also compared the model results to experimental utilization data and found that the use of Eq. (19) coupled to Eq. (11) resulted in

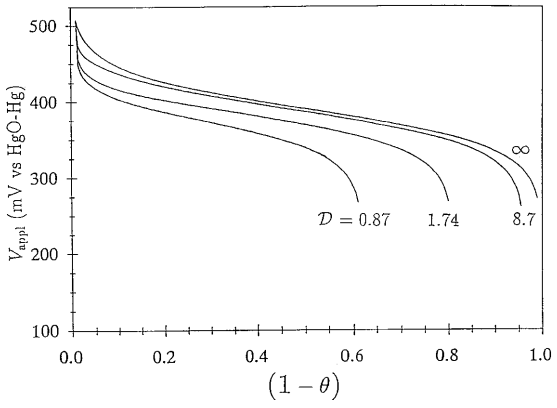

Fig. 7 Effect of proton mass-transfer resistance on nickel hydroxide discharge curves. As $\mathscr{D}$ (defined in Eq. 18) decreases, the mass-transfer resistance increases (reproduced from [35] by permission of The Electrochemical Society

excellent quantitative agreement. They also showed that a model that uses a constant diffusion coefficient does not agree even qualitatively with the data. For example, at a given current the utilization of the active material was found to be higher on charge than on discharge. This asymmetric behavior can only occur if the diffusion coefficient changes with SOC. Note that except for the functionality of Motupally et al. none of the diffusion coefficient values reported in Fig. 4 would fit the utilization versus current data.

The advantage of assuming D_{H^+} is constant is that there is an analytical solution to Eq. (9). Paxton and Newman [40] describe a procedure by which a constant diffusion coefficient can be estimated from a varying diffusion coefficient data. The authors [40] model the nickel hydroxide electrode assuming spherical particles, use the SOC-dependent diffusion coefficient [37], and generate a plot of average concentration versus surface concentration. They then attempt to evaluate a constant diffusion coefficient that averages this varying value by

two methods: (1) by performing a least squares fit and (2) by finding the diffusion coefficient that produces a curve that terminates at the same average concentration as the varying diffusion coefficient data. These average values of D_{H^+} are a function of discharge rate and electrode thickness. The authors then use their average diffusion coefficient values in a two-dimensional, nickel-cadmium cell model, which includes the porous electrode [26].

Electron conductivity and semiconductor effects

Some mathematical models of the active material have attempted to predict the potential drop across the active material by applying Ohm's law to the solid phase and assuming the pertinent conductivity was that of electrons [20–22, 27, 35]. Most of these models used SOC-dependent conductivity expressions of the form [56]:

$$\sigma = 0.1185\ \exp\left[-8.459(1-\theta)^4\right] \tag{20}$$

With this functionality, σ ranges from $0.1185\,\Omega^{-1}\,\mathrm{cm}^{-1}$ in the fully charged state to $2.5\times10^{-5}\,\Omega^{-1}\,\mathrm{cm}^{-1}$ in the discharged state (see Fig. 8). Although other conductivity expressions go even lower than 2.5×10^{-5} $\Omega^{-1}\,\mathrm{cm}^{-1}$, the trends predicted when using a SOC-dependent conductivity expression are similar to those shown in Fig. 9. In this figure, discharge curves are shown for different values of ohmic resistance, described using the parameter σ^* defined by Weidner and Timmerman [35] as:

$$\sigma^* = \frac{t_d \sigma RT}{F^2 c_{H^+,\max}\delta^2} \equiv \frac{\text{discharge time}}{\text{ohmic resistance}} \tag{21}$$

Figures 7 and 9 show that increasing either the diffusion resistance or the ohmic resistance results in a decrease in the utilization at high rates. While diffusion resistance

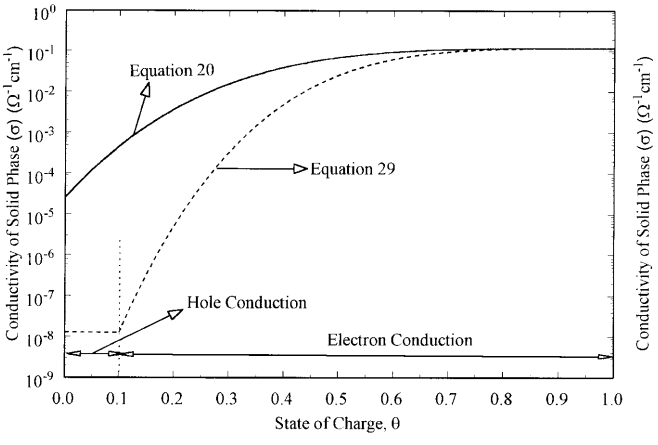

Fig. 8 Electronic conductivity of the nickel hydroxide electrode as a function of the state-of-charge. The *solid curve* denotes Eq. (20), while the *dotted line* denotes Eq. (29)

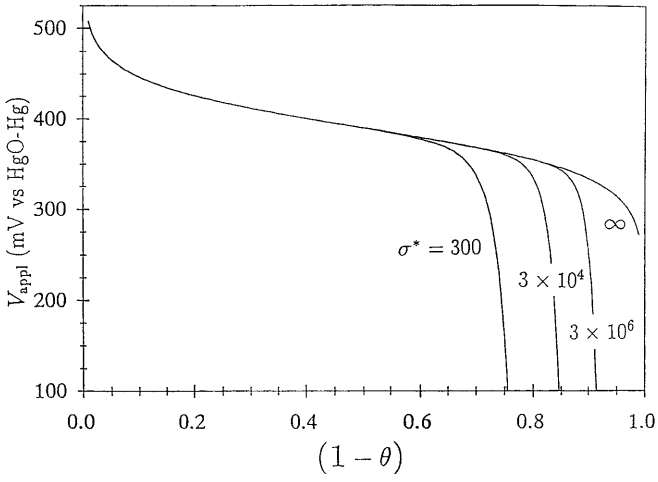

Fig. 9 Effect of ohmic resistance on nickel hydroxide discharge curves. As σ^* (defined in Eq. 21) decreases, the ohmic resistance increases. Note the similarity between Figs. 7 and 9 with a drop in utilization at high rates (reproduced from [35] by permission of The Electrochemical Society)

results in a decreased proton concentration at the film-electrolyte interface and hence a greater imposed potential, low conductivity results in a large ohmic drop across the film and hence a lower measured potential. In contrast, electronic conductivity had little effect on the voltage during the early portion of the discharge owing to the relatively low ohmic resistance.

While all the models described above assume the nickel hydroxide film is non-porous, Lanzi and Landau [42] modeled the thin film as a porous electrode. They studied the effect of electronic resistance on the reaction distribution and the ohmic drop. The authors used Ohm's law to describe the potential drop in the oxide, a modified Ohm's law (based on dilute solution theory) for the potential drop in solution, and a SOC-dependent Tafel expression for the kinetics. The authors assumed that the nickel reduction reaction was composed of three steps: (1) a reversible proton vacancy formation ($NiOOH^-$); (2) vacancy diffusion to the interface, which was assumed rate determining; and (3) a fast reduction reaction to form $Ni(OH)_2$. The vacancy diffusion assumed by Lanzi and Landau is analogous to the proton diffusion assumed by other authors. Assuming the oxide film to have low conductivity, the authors generate reaction distribution plots and show that the reaction is concentrated at the current collector at low states of charge. This occurs because the oxide is much less conductive compared to the solution, and hence the current transfers to the solution with little penetration into the oxide to avoid the high resistance. The authors derive a condition for the occurrence of the "layer discharge" (existence of a reaction zone) and suggest that if

$$a|i_{avg}|L^2 \gg \frac{\pi^2 RT(1-\varepsilon)\sigma}{2\alpha F\tau} \tag{22}$$

then layer discharge would occur.

Lanzi and Landau [42] also studied sinter failure in porous nickel plaques using the model and showed that the utilization decreases with increasing resistance of the solid phase. This increased resistance was accounted for by assuming that the sinter fracture results in decreased conductivity. The three important parameters that characterize the life and performance of the electrode are: (1) $a|i_{avg}|L^2$, (2) σ, and (3) f, the fraction of oxide that is damaged by sinter fracture. While decreasing the thickness increases the utilization, such an effect can also be achieved by increasing σ (by using additives). The authors also suggest that increasing the sinter strength or/and increasing the number of current collectors may lead to better electrodes.

Some investigators have tried to incorporate the semiconducting nature of the active material into their models. Two models, one based on continuum mechanics [57] and the other based on semiconductor theory [28], are reviewed in this paper. Nickel hydroxide is a p-type semiconductor where hole conduction dominates [58]. However, the charged material, β-NiOOH, has been reported to be a n-type semiconductor with electron conduction [59, 60]. Semiconductor materials could have transport limitations for the conducting species, and hence be the cause for limiting the rate capability of cells. Such an effect is common in liquid-junction solar cells [8].

Continuum models to describe the semiconductor effects use an approach similar to that used to model transport in electrolytes with electrons and holes considered as species. For example, in nickel hydroxide the transport of electrons, holes, and protons needs to be described along with the potential in the active material. Dilute solution approximations apply, as the doping levels of most semiconductors are small. Flux expressions can be developed that are analogous to those used in dilute solutions (see chapter 11 in Newman [8]), considering both diffusion and migration (termed ''drift''). The Nernst-Einstein approximation is used to relate the diffusion coefficient to the mobility, and Poisson's equation is used for the potential. Semiconductors have a homogeneous reaction where electrons-hole pairs are generated/recombined. This is expressed using rate expressions that account for the mechanism of the reaction. For example, Sinha [57] derives a rate expression for electron-hole and proton generation/recombination based on the assumption that the rate is close to equilibrium. The boundary conditions depend on the phenomena that occur at the semiconductor/metal interface and the semiconductor/electrolyte interface. For example, the Schottky barrier between the metal and the semiconductor can be modeled as an exponential expression (similar to Eq. 25) to relate the current and the potential. For a detailed review on using semiconductor theory to describe electrochemical systems, see Orazem and Newman [61, 62] and Newman [8]. For details on semiconductor physics, see Streetman [63] and Kittel [64].

Sinha [57] presented a detailed mathematical model of the nickel hydroxide electrode that incorporated porous electrode theory and concentrated solution theory to describe the electrode, and semiconductor physics to describe the nickel hydroxide layer. Sinha described the nickel oxidation and oxygen evolution reactions in his model and corrected the overpotentials for the voltage drop across the active material. In order to evaluate this voltage drop, the author [57] considered transport of electrons, holes, and protons with generation and recombination of charge carriers in the bulk of the semiconductor. Sinha identifies three mechanisms by which the reaction can proceed: (1) mobile protons and stationary electrons with a homogeneous reaction; (2) a reaction front whose direction depends on the relative rates of transport of the protons and electrons; and (3) a homogeneous reaction with both the electron and the proton having similar diffusion rates. Mechanism (1) is negated based on the fact that the electron can move through oxide materials. Depending on the relative transport rates of protons and electrons, mechanism (2) or (3) could dominate. Sinha models the system assuming case (3) to be dominant, under steady state conditions. The moving color front observed in Ni electrodes [65] suggests that mechanism (2) may be more appropriate. With the assumption that the hole conductivity dominates, the potential drop was expressed as:

$$\nabla\phi_l = -\frac{j_{in}}{\sigma} + \left(\frac{F}{\sigma}\right)\left(D_n\nabla c_n - D_p\nabla c_p - D_{H^+}\nabla c_{H^+}\right) \tag{23}$$

where the conductivity σ can be expressed in terms of the mobilities of the proton, electron, and hole. However, owing to lack of information of the solid state properties in the material (e.g., diffusion coefficient), the authors simplify their model for a case where the electron and hole concentrations are constant and express their potential drop as

$$\nabla\phi_l = -\frac{j_{in}}{\sigma} - \left(\frac{F}{\sigma}\right)D_{H^+}\nabla c_{H^+} \tag{24}$$

Note that this equation is similar to Eq. 11.5 in Newman [8] for the current in a dilute solution due to diffusion and migration. To solve Eq. (24), Sinha assumed that at the film/electrolyte interface the concentration of NiOOH is a constant and is the same as that of the initial concentration. However, as the discharge proceeds, the concentration of protons decreases and hence a more appropriate boundary condition would be to equate the flux of protons to a current. How this effects the results of the model is not clear.

Owing to lack of experimental data, this model was not used to study the effect of the various solid state parameters on the performance. However, in the years since the development of the model, experimental data have provided information on some of these parameters. For example, the diffusion coefficient of protons [36–38] (and hence the mobility) and the band gap [58, 60] (needed for understanding reaction mechanisms) have been estimated.

While Sinha [57] assumes the active material to be predominantly p-type, Barnard et al. [28] considered both the n and p carriers to explain the so-called second discharge plateau observed frequently during the discharge of nickel electrodes [3, 4, 66–78]. While the first plateau occurs due to the nickel oxidation/reduction reaction via reaction (2), the second plateau appears approximately 400 mV cathodic of it and has been reported to have as much as 50% of the capacity of the first plateau [3]. However, the potential where it is extracted is too low to be of any practical importance.

There is considerable debate as to the origin of this second discharge plateau and the literature can be divided into three distinct theories, namely: (1) a decrease in electronic conductivity as the material discharges, resulting in a need for a greater driving force [28, 41, 74]; (2) reduction of oxygen at the nickel electrode (reverse of reaction 3) [66, 67, 72, 76]; and (3) discharging of an intrinsically less active material [e.g., $Ni_3O_2(OH)_4$ or $Ni_3O_4 \cdot xH_2O$] that is formed during discharge [41, 68–72, 75, 77, 78].

Barnard et al. [28] considered the second discharge plateau to arise from a mixed p-n semiconducting material under reverse bias conditions. As mentioned earlier, the nickel hydroxide electrode is a p-type semiconductor. As the electrode is charged, n-type carries are generated, leading to the formation of p-n junctions. For this system, the current voltage response can be expressed as [79]:

$$I = \frac{1}{L}\frac{RT}{F}\left\{\sigma_e^0\left[1 - \exp\left(-\eta\frac{F}{RT}\right)\right] + \sigma_h^0\left[\exp\left(\eta\frac{F}{RT}\right) - 1\right]\right\} \quad (25)$$

Barnard assumed that the conductivity of electrons depends on the SOC and used the relation:

$$\log(\sigma_e^0) \propto \log\left(\frac{N_i^{3+}}{N_o}\right) \quad (26)$$

During discharge, Eq. (25) simplifies for large η to:

$$I = \frac{1}{L}\frac{RT}{F}\left[\sigma_h^0\ \exp\left(\eta\frac{F}{RT}\right) + \sigma_e^0\right] \quad (27)$$

When $\sigma_h^0 \ll \sigma_e^0$, the current due to electrons reaches a plateau until the hole current takes over the conduction process. This causes the secondary discharge plateau. Therefore, Barnard suggested that the second discharge plateau can be thought of as the discharge of the material with oxidation state less than 2.25. On charge, Eq. 25 reduces to [79]

$$I = \frac{1}{L}\frac{RT}{F}\sigma_e^0\left[1 - \exp\left(-\eta\frac{F}{RT}\right)\right] \quad (28)$$

and no secondary plateau is expected as the current is carried predominantly by electrons.

Such an approach was used by Mao et al. [27] to model the second discharge plateau in a nickel-hydrogen cell using a comprehensive cell model which incorporates proton diffusion and porous electrode theory using a pseudo two-dimensional approach. They considered the conductivity of the active material to be a continuous function until a state-of-charge of 0.1. At this point, the authors assumed a discontinuity in the conductivity at a constant low value. For the conductivity expressions the authors used:

$$\sigma = \begin{cases} 0.1185\ \exp\left[-24.45(1-\theta)^4\right] & 1 \geq \theta \geq 0.1 \\ 0.1185\ \exp\left[-24.45(0.9)^4\right] & \theta \leq 0.1 \end{cases} \quad (29)$$

which is analogous to Eq. (20) and is also plotted in Fig. 5. This can be interpreted as a model that incorporates the first explanation of the second plateau given above, where the conductivity of the active material decreases steadily during discharge, as predicted by Eq. (29), between the SOC of 1 and 0.1. At this low SOC, the conduction in the film shifts from electron conducting to hole conducting and the hole conductivity is a constant at $\sim 1.2 \times 10^{-8}\,\Omega^{-1}\,cm^{-1}$. This low conductivity results in a greater ohmic drop and hence the potential where the reaction occurs is lower.

In contrast to the models that assume the conductivity to be the cause for the second discharge plateau, the model by De Vidts et al. [22] was successful in predicting the second discharge plateau for a Ni-H_2 cell by considering the oxygen reduction reaction (reverse of reaction 3). Although the oxygen reduction reaction has been included in previous models for the Ni-Cd battery developed by the authors [16–18, 20], they do not predict a second plateau. De Vidts et al. [22] explain this by suggesting that the oxygen generated in the positive electrode in a Ni-Cd cell is transported to the negative electrode easily as the mass transfer resistance is low. At the negative electrode, the oxygen is reduced. Hence, not much dissolved oxygen is present in these cells. However, in a Ni-H_2 cell the model predicts that there is ample dissolved oxygen present to sustain the reaction. De Vidts et al. [22] simulated the effect of oxygen pressure on the second discharge plateau and predicted a change in potential to less negative values on increasing the pressure. In addition, the model predicts that an increase the pressure would result in a bigger second plateau, as there is more oxygen in the cell.

However, recent evidence has suggested that oxygen may not be the sole cause for the second plateau [75, 77, 78], although one cannot neglect it in evaluating the capacity as it occurs at the same potential [76]. These authors [75, 77, 78] seem to agree that the second plateau is caused by an intermediate phase but differ on the composition of the phase. While Sac-Epée et al. [75, 77] suggest that the second plateau occurs due to the direct conversion of the γ(III) phase of the β(II) phase, Léger et al. [78] observe this plateau even in the absence of the γ phase and attribute it to a poorly electronically

conductive material. However, the recent research is based on electrodes devoid of cobalt additives. Explanations as to the cause of the second plateau in the presence of cobalt are still lacking.

Models for the nickel hydroxide redox processes

Most models to date have assumed reactions (1) and (2) to be representative of the redox processes that occur in the active material. However, depending on the preparation conditions, the electrochemical signatures of the active material (e.g., number of electrons transferred, charge and discharge voltage) are known to vary. In addition, variations are also seen during cycling, standing, and overcharge. Many of these variations are thought to occur owing to the existence of two different crystal phases of the active material. Bode and coworkers [4] summarized the complex chemical and electrochemical processes in the nickel electrode as follows:

$$\begin{array}{ccc} \alpha\text{-Ni(OH)}_2 & \underset{\text{discharge}}{\overset{\text{charge}}{\rightleftharpoons}} & \gamma\text{-NiOOH} \\ \Big\downarrow \text{dehydration} & & \Big\uparrow \text{overcharge} \\ \beta\text{-Ni(OH)}_2 & \underset{\text{discharge}}{\overset{\text{charge}}{\rightleftharpoons}} & \beta\text{-NiOOH} \end{array} \qquad (30)$$

These reactions are not written as balanced reactions, but rather to illustrate the relationship between the various phases. The hydrated, non-close-packed phase, termed α-$Ni(OH)_2$, is unstable and dehydrates to the anhydrous close-packed phase, termed β-$Ni(OH)_2$, in concentrated alkali solution. oxidation of β-$Ni(OH)_2$ results in the formation of β-NiOOH while oxidation of α-$Ni(OH)_2$ results in γ-NiOOH. The β phase converts to the γ phase on overcharge, as Ni(III) is converted to Ni(IV). The α-γ reaction is considered to have greater electron transfers compared to the β-β reaction. In addition, the α-γ reaction is considered to involve intercalation of potassium ions during charge [28, 80].

The qualitative mechanism given by Eq. (30) has been used to develop a quantitative description of these redox process. For example, Timmerman et al. [25] used the following redox reactions in their porous-electrode model:

$$\alpha\text{-}[Ni(OH)_2] + 1.5OH^- \underset{\text{discharge}}{\overset{\text{charge}}{\rightleftharpoons}} \gamma\text{-}[NiOOH] + 1.5H_2O + 1.5e^- \qquad (31)$$

$$\beta\text{-Ni(OH)}_2 + OH^- \underset{\text{discharge}}{\overset{\text{charge}}{\rightleftharpoons}} \beta\text{-NiOOH} + H_2O + e^- \qquad (32)$$

$$\beta\text{-NiOOH} \xrightarrow{\text{overcharge}} \gamma\text{-NiOOH} + 0.5e^- \qquad (33)$$

$$\alpha\text{-Ni(OH)}_2 \xrightarrow{\text{dehydration}} \beta\text{-Ni(OH)}_2 \qquad (34)$$

Although the results from their multiple phases model were preliminary, Timmerman et al. [25] showed that a second plateau observed on charge, close to the oxygen evolution plateau, can be modeled by using the β to γ overcharge reaction. Thaller and Zimmerman [81] include potassium uptake in the γ-phase formation reaction and have showed the change in KOH concentration across the cell as a function of the discharge rate.

However, many researchers have reported redox reactions that are intermediate to those shown in reactions (31) and (32) [80, 82–84] and considerable confusion exists as to the actual mechanism of the reactions under different cycling conditions. For example, it has been observed in thin films that the $1.67e^-$ transfer is possible only on the first charge and subsequent charge/discharge yield only 1 electron [80]. In addition, the structure of the electrochemically active phases are the subject of debate. Figure 10 presents a schematic of the Bode diagram shown to represent the lattice stacking. While the β-β phase is close-packed with a small c spacing of ~ 4.6Å, the α phase is non-close-packed with a larger c spacing. The γ phase is similar to the α phase in that it has a larger c spacing ($\sim$7 Å). However, Raman spectra on the electrodes have indicated that the four electrochemically active materials are of the same non-close-packed crystal structure [85–90] with "...ABBCCA..." stacking (Fig. 11) with one NiOOH formulae unit in the unit cell. Other structure like NiO_2 or $Ni_2O_3 \cdot H_2O$ were not representative of the active mass. This is in contrast to a manganese dioxide

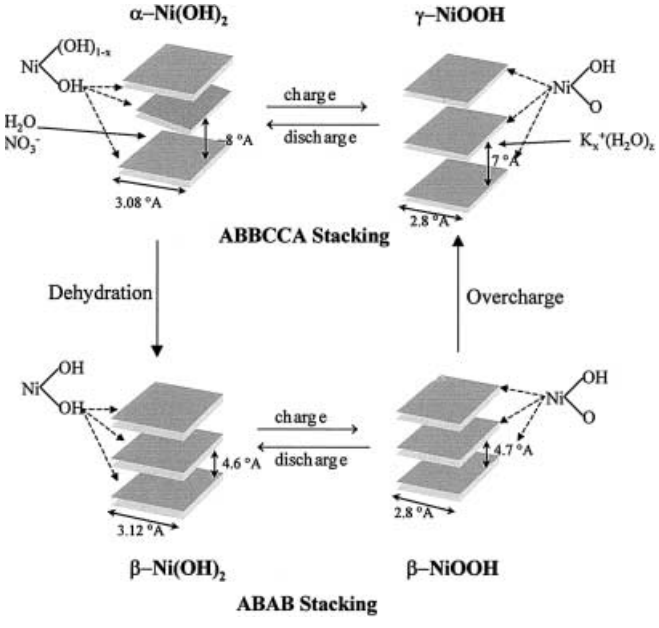

Fig. 10 Schematic of the layer stacking of the different phases in the Bode diagram (reaction 30) (based, in part, on [75] and [95] by permission of The Electrochemical Society)

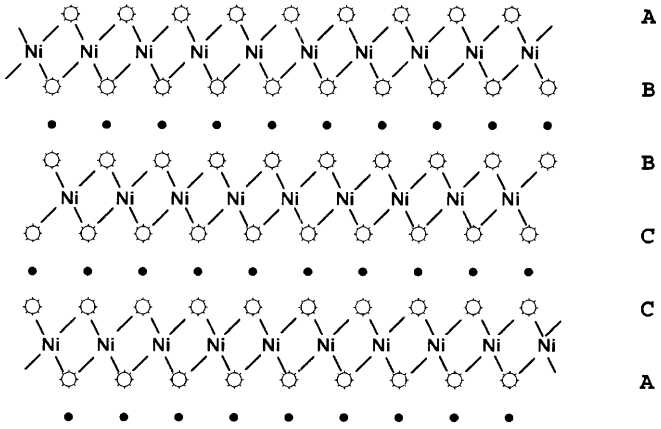

Fig. 11 Schematic of the "...ABBCCA..." non-close-packed, oxygen-layer stacking sequence observed for γ-NiOOH in the $R\bar{3}m$ [85] space group (○ = oxygen, • = hydrogen, Ni = nickel). This γ-type structure is the prototype for the layer stacking in charged and discharged active mass [85] (reproduced from [89] by permission of The Electrochemical Society)

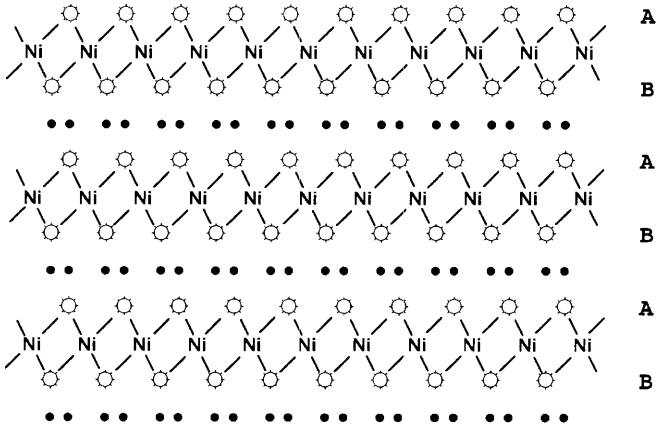

Fig. 12 Schematic of the "...ABAB..." close-packed, oxygen-layer stacking sequence observed for β-$Ni(OH)_2$ in the $P\bar{3}m1$ [96] space group (○ = oxygen, • = hydrogen, Ni = nickel) (reproduced from [89] by permission of The Electrochemical Society)

electrode, analyzed by Ruetschi [91], where the unit cell consists of MnO_2 units. In addition, the close-packed phase with "...ABAB..." stacking (Fig. 12) is electrochemically unstable. This deviates from the Bode diagram where the close-packed β phase is considered a stable electrochemically active phase. This alternative scheme can be represented in the form of a modified Bode diagram as [88, 89]:

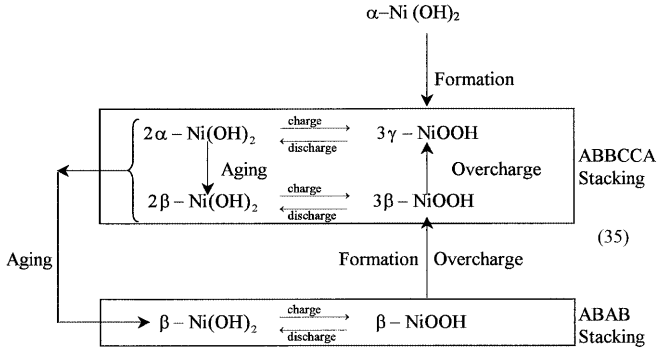

Again, these reactions are not written as balanced reactions, but rather to illustrate the relationship between the various redox cycles. According to this scheme, a cathodically deposited $Ni(OH)_2$ film has a "... ABBCCA ..." non-closed-packed structure and is green in color and is designated as the α phase. On charging this material, the film oxidizes to the 3γ phase, which is black. Subsequent charge/discharges result in the film converting from the 3γ phase to the 2α phase, with the film color remaining black. Aging of this material can lead to the 2β-3β cycle, which upon overcharge converts back to the 2α-3γ cycle. While it is possible to make materials with the close-packed structure ("... ABAB ..." stacking), the material is unstable and reverts back to the non-close-packed scheme on overcharge.

Loyselle et al. [90] used a point defect approach to describe the active material and proposed that the difference between the two electrochemical reactions represented in the upper rectangle of Eq. (35) was the level of defects. For example, the 2α-3γ cycle was observed to have 25% nickel defects, while the 2β-2β cycle has 11% defects, yet the same crystal structure. The defects are either occupied by protons, potassium ions, or are left vacant. The modified Bode diagram, however, is also simplistic in that it implies a limited number of redox cycles. In reality, the reaction changes continuously as the defect parameters change. Therefore, it is beneficial to express the continuum of reactions using the following redox expression [43, 89]:

$$\left[\mathrm{Ni(K)}_{\frac{y_1}{(1-x_1)}}(n_1\mathrm{H})_{\frac{x_1-y_1}{1-x_1}}\right]\mathrm{O}_{\frac{2}{1-x_1}}\mathrm{H}_{\frac{2}{1-x_1}}\cdot X_{\mathrm{W}_1}\mathrm{H_2O}+\lambda_1\mathrm{OH}^-+\lambda_2\mathrm{K}^+ \underset{\text{discharge}}{\overset{\text{charge}}{\rightleftharpoons}} \left[\mathrm{Ni(K)}_{\frac{y_2}{(1-x_2)}}(n_2\mathrm{H})_{\frac{x_2-y_2}{1-x_2}}\right]\mathrm{O}_{\frac{2}{1-x_2}}\mathrm{H}_{\frac{1}{1-x_2}}\cdot X_{\mathrm{W}_2}\mathrm{H_2O} + \lambda_3\mathrm{H_2O}+\lambda_4\mathrm{e}^- \quad (36)$$

where

$$\lambda_1 = \left[\frac{n_1(x_1-y_1)-2}{(1-x_1)} - \frac{n_2(x_2-y_2)-3}{(1-x_2)}\right]$$

$$\lambda_2 = \left[\frac{y_2}{(1-x_2)} - \frac{y_1}{(1-x_1)}\right]$$

$$\lambda_3 = \left[\frac{n_1(x_1-y_1)}{(1-x_1)} - \frac{n_2(x_2-y_2)-1}{(1-x_2)}\right] + X_{\mathrm{W}_1} - X_{\mathrm{W}_2}$$

$$\lambda_4 = \left[\frac{3-y_2-n_2(x_2-y_2)}{(1-x_2)} - \frac{2-y_1-n_1(x_1-y_1)}{(1-x_1)}\right]$$

where

$$x_i = \frac{\text{number of Ni vacancies}}{\text{total number of Ni lattice sites}}$$

$$y_i = \frac{\text{number of Ni vacancies occupied by } K^+}{\text{total number of Ni lattice sites}}$$

$$n_i = \frac{\text{number of } H^+}{\text{number of Ni vacancies not occupied by } K^+}$$

$$X_{w_i} = \frac{\text{number of water molecules}}{\text{total number of Ni lattice sites}}$$

Note that reaction (36) represents the two end-point materials during a charge and discharge. The continuous changes that occur during the charge or discharge can also be represented using an analogous notation.

Equation (36) can be used to represent each reaction shown in the modified Bode diagram. As stated earlier, Loyselle et al. [90] estimated that the 2α-3γ cycle has a defect content, x, of 0.25 and the 2β-3β cycle has a lower defect content of 0.11. From reaction (36), three expressions analogous to reactions (31)–(33) are obtained by substituting values for the defect parameters. The 2α-3γ cycle is obtained by substituting $x_1 = x_2 = y_2 = 0.25,\ n_1 = 0$ and $y_1 = 0$ into reaction (36) to give

$$\alpha\text{-}\left[Ni^{2.67}(V_{Ni})_{0.33}\right]O_{2.67}H_{2.67} + 1.33OH^- + 0.33K^+ \underset{\text{discharge}}{\overset{\text{charge}}{\rightleftharpoons}} \gamma\text{-}[Ni^{3.67}(K)_{0.33}]O_{2.67}H_{1.33} + 1.33H_2O + 1e^- \quad (37)$$

where the superscripts on the nickels represent their oxidation state and V_{Ni} represents a nickel vacancy that contains neither a potassium nor a hydrogen ion (i.e., $n_i = 0$). The 2β-3β cycle is obtained by substituting $x_1 = x_2 = 0.11,\ n_1 = 0,\ y_1 = y_2 = 0$ and $n_2 = 1$ to give:

$$\beta\text{-}\left[Ni^{2.25}(V_{Ni})_{0.12}\right]O_{2.25}H_{2.25} + OH^- \underset{\text{discharge}}{\overset{\text{charge}}{\rightleftharpoons}} \beta\text{-}\left[Ni^{3.25}(H)_{0.12}\right]O_{2.25}H_{1.12} + H_2O + 1e^- \quad (38)$$

Note that the defect model predicts that both the α-γ and β-β cycles involve $1e^-$ transfers. The $1.67e^-$ electron transfer is accounted for in a formation reaction obtained by substituting $x_1 = x_2 = y_2 = 0.25,\ n_1 = 2$, and $y_1 = 0$ into Eq. (36) to give

$$\left[Ni^{2.0}(2H)_{0.33}\right]O_{2.67}H_{2.67} + 2OH^- + 0.33K^+ \xrightarrow{\text{formation}} \left[Ni^{3.67}(K)_{0.33}\right]O_{2.67}H_{1.33} + 2H_2O + 1.67e^- \quad (39)$$

The β to γ overcharge reaction is written as

$$\left[Ni^{3.25}(H)_{0.12}\right]O_{2.25}H_{1.12} + 0.75OH^- + 0.33K^+ \xrightarrow{\text{overcharge}} \left[Ni^{3.67}(K)_{0.33}\right]O_{2.67}H_{1.33} + 0.33H_2O + 0.42e^- \quad (40)$$

Note that when $y_2 = x_2$ all the vacancies are occupied by potassium ions and hence the value of n_2 is irrelevant.

According to reaction (36), the charge and discharge of the electrode involves a change in oxidation state of nickel and a change in mass of the active material due to the incorporation of cations, protons, and water. The extent of these changes depend on the defect parameters of the material. Srinivasan et al. [43] measured the mass change of nickel hydroxide films while simultaneously measuring the capacity using an electrochemical quartz crystal microbalance (EQCM) and related them to the defect parameters. Using the experimental mass change and capacity data along with the defect model, the authors detailed a procedure by which the defect parameters could be extracted. The procedure was used to understand four experimentally observed phenomenon in the nickel electrode, namely (1) $1.67e^-$ transfer in the first charge while subsequent charges lead to $1e^-$ transfer [80], (2) $1e^-$ transfer for the first discharge [80], (3) a steady decrease in capacity on both charge and discharge on cycling [92, 93], and (4) an increase in the total mass of the film on cycling [94].

Using the defect model, the authors [43] reasoned that the cause of the capacity decrease on cycling is due to the incomplete incorporation of potassium ions into (or near) the nickel vacancy. The cause for the four phenomenon described above can be summarized as:

1. A cathodically deposited α nickel hydroxide film has a defect content of 0.25. During the first charge, the two protons from the nickel vacancy de-intercalate and in turn a K^+ ion occupies the vacancy, resulting in a 1.67 electron transfer.
2. During discharge, the K^+ de-intercalates and the vacancy is left vacant, resulting in a 1 electron transfer.
3. As the film is cycled, the K^+ content of the film decreases and the lattice appears to be filled with two protons instead, thus leading to a lower oxidation state of Ni in the charged state and a drop in capacity.
4. The water content of the film appears to increase on cycling, thus leading to an increase in the total mass of the film.

Conclusions

A review of the continuum models developed to describe the nickel hydroxide active material was presented. The review includes models that describe the equilibrium potential, proton diffusion, electronic conductivity and semiconducting effects, and reactions in the solid phase. The methodology used in developing the models, and their relative strengths/weaknesses, were discussed. More comprehensive models that describe the solid state reactions in the active material and that account for the semiconducting aspects of the material are needed. In addition, model-to-experimental comparisons have to be undertaken to estimate accurately the physical parameters that are required for these models to be predictive.

Glossary

a	interfacial surface area per unit volume ($cm^2\ cm^{-3}$)
$a_{Ni(OH)}$	activity of nickel hydroxide (mol cm^{-3})
a_{NiOOH}	activity of nickel oxyhydroxide (mol cm^{-3})
A	intercalation constant in one-parameter Margules corrected Nernst equation (in Eq. 5)
A_0, B_0	intercalation constants in two-parameter Margules corrected Nernst equation (in Eq. 6)
c_{eq}	equilibrium proton concentration (mol cm^{-3})
c_n	concentration of electrons in the nickel hydroxide film (mol cm^{-3})
c_p	concentration of holes in the nickel hydroxide film (mol cm^{-3})
c_{ref}	reference concentration (mol cm^{-3})
c_{H^+}	concentration of protons (mol cm^{-3})
$c^0_{H^+}$	initial proton concentration (mol cm^{-3})
$c_{H^+,max}$	maximum proton concentration ($cm^3\ s^{-1}$)
D_{H^+}	solid state diffusion coefficient of protons ($cm^2\ s^{-1}$)
$D_{Ni(OH)_2}$	diffusion coefficient of protons in $Ni(OH)_2$ (0% SOC) ($cm^2\ s^{-1}$)
D_{NiOOH}	diffusion coefficient of protons in NiOOH (100% SOC) ($cm^2\ s^{-1}$)
D_n	diffusion coefficient of electrons ($cm^2\ s^{-1}$)
D_p	diffusion coefficient of holes ($cm^2\ s^{-1}$)
$\mathscr{D}$	dimensionless mass transfer resistance defined in Eq. (18)
E	electrode potential (V)
E°	standard potential (V)
f	fraction of oxide that is damaged by sinter fracture
F	Faraday's constant (96 487 C $equiv^{-1}$)
i_{avg}	average current density over the electrode thickness (A cm^{-2})
I	current density (A cm^{-2})
I_0	dimensionless charge transfer resistance defined in Eq. (17)
$i_{0,ref}$	exchange current density evaluated at reference conditions (A cm^{-2})
j_{in}	pore wall flux density of species i(mol $cm^{-2}\ s^{-1}$)
L	distance from current collector to the site of reaction used in Eq. (25) (cm)
n_i	number of protons divided by number of Ni vacancies not occupied by K^+
N_0	Avagadro's number ($6.023 \times 10^{23}\ mol^{-1}$)
Ni^{3+}	number of Ni^{3+} ions injected into $Ni(OH)_2$ in Eq. (26)
R	universal gas constant (8.3143 J $mol^{-1}\ K^{-1}$)
T	temperature (K)
t	time (s)
t_d	time required to discharge to maximum capacity (s)
x_i	moles of vacancies per mole of lattice sites
X_{wi}	moles of water per mole of nickel
y	second dimension (cm)
y_i	moles of vacancies occupied by potassium ions per mole of lattice sites

Greek

α	transfer coefficients
δ	thickness of the nickel hydroxide film (cm)
ε	porosity
ϕ_1	electric potential in the matrix phase (V)
η	overpotential (V)
θ	state-of-charge or dimensionless proton concentration
θ^0	initial state-of-charge
σ	conductivity of the matrix phase ($\Omega^{-1}\ cm^{-1}$)
σ^*	dimensionless ohmic resistance defined in Eq. 21
σ^0_e	specific conductivity of electrons ($\Omega^{-1}cm^{-1}$)
σ^0_h	specific conductivity of holes ($\Omega^{-1}\ cm^{-1}$)
τ	tortuosity factor

Subscript

1	discharged phase
2	charged phase

Acknowledgements The authors gratefully acknowledge the financial support from the Office of Research and Development of the United States Central Intelligence Agency and the US Department of Energy under cooperative agreement number DE-FC02-91ER75666. Dr. Y.-M. Tarascon and Prof. Bahne C. Cornilsen are acknowledged for permission to reproduce Fig. 10 and Figs. 11 and 12, respectively. The Electrochemical Society is acknowledged for permission to reproduce Figs. 5–7 and 9–12.

References

1. Linden D (1984) Handbook of batteries and fuel cells. McGraw-Hill, New York
2. McBreen J (1990) The nickel oxide electrode. In: White RE, Bockris JO'M, Conway BE (eds) Modern aspects of electrochemistry, vol 21. Plenum Press, New York, pp 29–63
3. Milner PC, Thomas UB (1967) The nickel cadmium cell. In: Tobias CW (ed) Advances in electrochemistry and electrochemical engineering, vol 5. Interscience, New York, pp 1–86
4. Bode H, Dehmelt K, Witte J (1966) Electrochim Acta 11: 1079
5. Newman J, Bennion D, Tobais CW (1965) Ber Bunsenges Phys Chem 69: 608
6. Newman J, Bennion D, Tobais CW (1966) Ber Bunsenges Phys Chem 70: 493
7. Newman J, Chapman TW (1973) AIChE J 19: 343
8. Newman J (1973) Electrochemical systems. Prentice-Hall, Englewood Cliffs, NJ
9. Bennion DN (1964) Phenomenon at a gas-electrode-electrolyte interface. PhD Thesis, University of California, Berkeley
10. Newman J, Tiedmann W (1975) AIChE J 21: 25
11. Posey FA (1964) J Electrochem Soc 111: 1173
12. DeLevie R (1967) Electrochemical response of rough and porous electrodes. In: Tobais CW (ed) Advances in electrochemistry and electrochemical engineering, vol 6. Interscience, New York, pp 329–397
13. Micka K, Rousar R (1980) Electrochim Acta 25: 1085
14. Micka K, Rousar R (1982) Electrochim Acta 27: 765

15. Choi KW, Yao NP (1979) A mathematical model for porous nickel electrodes in zinc/nickel oxide cells. In: Gross S (ed) Proceedings of the symposium on battery design and optimization. (The Electrochemical Society proceedings series, vol PV 79-1) The Electrochemical Society, Pennington, NJ, p 62
16. Fan D, White RE (1991) J Electrochem Soc 138: 17
17. Fan D, White RE (1991) J Electrochem Soc 138: 2952
18. Fan D (1991) Mathematical modeling of a sealed nickel-cadmium cell. PhD Thesis, Texas A&M University
19. Bouet J, Richard F, Blanchard P (1990) A discharge model for the nickel hydroxide positive electrode. In: Corrigan DA, Zimmerman AH (eds) Proceedings of the symposium on nickel hydroxide electrodes. (The Electrochemical Society proceedings series, vol PV 90-4) The Electrochemical Society, Pennington, NJ, p 260
20. De Vidts P (1995) J Electrochem Soc 142: 1509
21. De Vidts P (1995) Mathematical modeling of a nickel/hydrogen cell. PhD Thesis, Texas A&M University
22. De Vidts P, Delgado J, White RE (1996) J Electrochem. Soc 143: 3223
23. De Vidts P, Delgado J, Wu B, See D, Kosanovich K, White RE (1998) J Electrochem Soc 145: 3874
24. RatnaKumar BV, Timmerman P, Sanchez C, Stefano SD, Halpert G (1996) J Electrochem Soc 143: 803
25. Timmerman P, Ratnakumar BV, Stefano SD (1996) Modeling of nickel hydroxide electrode containing multiple phases. In: Bennet PD, Gross S (eds) Aqueous batteries. (The Electrochemical Society proceedings series, vol PV 96-16) The Electrochemical Society, Pennington, NJ, p 130
26. Paxton B, Newman J (1997) J Electrochem Soc 144: 3818
27. Mao Z, De Vidts P, White RE, Newman J (1994) J Electrochem Soc 141: 54
28. Barnard P, Randell CF, Tye FL (1980) J Appl Electrochem 10: 127
29. Jain M, Elmore AL, Matthews MA, Weidner JW (1998) Electrochim Acta 43: 2649
30. Ta KP (1997) Solid-state diffusion coefficient measurement and modeling of intercalation materials. PhD Thesis, University of California, Berkeley
31. MacArthur DM (1970) J Electrochem Soc 117: 422
32. Zhang C, Park S (1987) J Electrochem Soc 134: 2966
33. MacArthur DM (1970) J Electrochem Soc 117: 729
34. Briggs GWD, Snodin PR (1982) Electrochim Acta 27: 565
35. Weidner JW, Timmerman P (1994) J Electrochem Soc 141: 346
36. Motupally S (1994) Measurement of diffusion coefficient of protons in nickel hydroxide films as a function of state of charge. PhD Thesis, University of South Carolina
37. Motupally S, Streinz CC, Weidner JW (1995) J Electrochem Soc 142: 1401
38. Ta KP, Newman J (1998) J Electrochem Soc 145: 3860
39. Motupally S, Streinz CC, Weidner JW (1998) J Electrochem Soc 145: 29
40. Paxton B, Newman J (1996) J Electrochem Soc 4: 1287
41. Barnard R, Crickmore GT, Lee JA, Tye FL (1980) J Appl Electrochem 10: 61
42. Lanzi O, Landau U (1991) J Electrochem Soc 138: 2527
43. Srinivasan V, Cornilsen BC, Weidner JW (1999) The application of point defect chemistry in characterizing the redox processes in the nickel hydroxide electrode. In: Cieslak WR (ed) Selected battery topics. (The Electrochemical Society proceedings series, vol PV 98-15) The Electrochemical Society, Pennington, NJ, p 31
44. Conway BE, Bourgault PL (1959) Can J Chem 37: 292
45. Tillement O, Quarton M (1993) J Electrochem Soc 140: 1870
46. Conway B, Gileadi E (1962) Can J Chem 40: 1933
47. Ta KP, Newman J (1999) J Electrochem Soc 146: 2769
48. Lukovtsev PD, Slaidin GJ (1971) Electrochim Acta 6: 17
49. Zimmerman AH, Effa PK (1985) Nickel hydroxide active material densities. In: The Electrochemical Society extended abstracts. (The Electrochemical Society proceedings series, vol 85-2) The Electrochemical Society, Pennington, NJ, pp 43
50. Lang G, Inzelt G (1999) Electrochim Acta 44: 2037
51. Tribollet B, Newman J (1984) J Electrochem Soc 131: 2780
52. Fuller T (1992) Solid polymer-electrolyte fuel cells. PhD Thesis, University of California, Berkeley
53. Viner AS, Fedkiw PS (1990) J Electrochem Soc 137: 1435
54. Bard AJ, Faulkner LR (1980) Electrochemical methods: fundamentals and applications. Wiley, New York
55. Yoon Y-G, Pyun S-I (1997) Electrochim Acta 42: 2465
56. Antonenko PA, Barsukov VZ, Krapivnii NG, Sagoyan N (1972) Vopr Khim Khim Tekhnol Chem Abstr vol 78, 1973, 131222g
57. Sinha M (1982) A mathematical model for the porous nickel hydroxide electrode. PhD Thesis, University of California, Los Angeles
58. Madou MJ, McKubre MCH (1983) J Electrochem Soc 130: 1056
59. Tuomi D (1965) J Electrochem Soc 112: 1
60. Carpenter MK, Corrigan DA (1989) J Electrochem Soc 136: 1022
61. Orazem ME, Newman J (1984) J Electrochem Soc 131: 2569
62. Orazem ME, Newman J (1986) Photoelectrochemical devices for solar energy conversion. In: White RE, Bockris JO'M, Conway BE (eds) Modern aspects of electrochemistry, vol 18. Plenum Press, New York, pp 61–112
63. Streetman BG (1995) Solid state electronic devices. Prentice-Hall, New York
64. Kittel C (1986) Introduction to solid state physics. Wiley, New York
65. Barnard R, Randell CF, Tye FL (1980) J Appl Electrochem 10: 109
66. Zedner J (1906) Z Elektrochem 12: 463
67. Forester F (1907) Z Elektrochem 13: 414
68. Rollet AP (1930) Ann Chim 13: 217
69. Besson J (1947) Ann Chim 2: 527
70. Glemser O, Einerhand J (1950) Z Elektrochem 54: 302
71. Wakkard SESE, Emara ES (1953) J Chem Soc 4: 3504
72. Falk SU (1960) J Electrochem Soc 8: 659
73. Klaptse B, Mrha J, Micka K, Jindra J, Marecek V (1979) J Power Sources 4: 349
74. Zimmerman AH, Effa PK (1984) J Electrochem Soc 129: 983
75. Sac-Epee N, Palacin MR, Beaudoin B, Delahaye-Vidal A, Jamin T, Chabre Y, Tarascon J-M (1997) J Electrochem Soc 144: 3896
76. Motupally S, Jain M, Srinivasan V, Weidner JW (1998) J Electrochem Soc 145: 34
77. Sac-Epee N, Palacin MR, Delahaye-Vidal A, Chabre Y, Tarascon J-M (1998) J Electrochem Soc 145: 1434
78. Leger C, Tessier C, Menetrier M, Denage C, Delmas C (1999) J Electrochem Soc 146: 924
79. Wagner JB (1973) Electronic conductivity, mobility and double layer capacity in solid state electrolytes. In: van Gool W (ed) Fast ion transport in solids, solid state batteries and devices. North-Holland Amsterdam, p 489
80. Corrigan DA, Knight SL (1989) J Electrochem Soc 136: 613
81. Thaller LH, Zimmerman AH (1996) J Power Sources 63: 53
82. Arthur DMM (1970) J Electrochem Soc 117: 422
83. Cheek GT, O'Grady WE (1997) J Electroanal Chem 421: 173
84. Carbonio RE, Macagno VA, Arvia AJ (1984) J Electroanal Chem 177: 217
85. Cornilsen BC, Karjala PJ, Loyselle PL (1988) J Power Sources 22: 351
86. Cornilsen BC, Shan X, Loyselle PL (1990) J Power Sources 29: 453
87. Cornilsen BC, Shan X, Loyselle PL (1990) The structure and reactions of the nickel electrode. In: Corrigan DA, Zimmerman AH (eds) Proceedings of the symposium on nickel hydroxide electrodes. (The Electrochemical Society proceedings series, vol PV 90-4) The Electrochemical Society, Pennington, NJ, p 82
88. Cornilsen B, Cai X, Tanbug R, Meitzner G (1997) Nickel electrode oxidation states, the presence of Ni(IV) and one-electron transfer in oxidized and reduced materials. In: Bennett PD, Gross S (eds) Aqueous batteries. (The Electrochemical Society proceedings series, vol PV 96-16) The Electrochemical Society Pennington, NJ, p 88

89. Cornilsen BC (1999) The nonstoichiometric solid solution structural model for nickel electrode active mass. In: Cieslak WR (ed) Selected battery topics. (The Electrochemical Society proceedings series, vol PV 98-15) The Electrochemical Society, Pennington, NJ, p 23
90. Loyselle PL, Karjala PJ, Cornilsen BC (1986) A point defect model for nickel electrode structures. In: Selman RJ, Maru HC (eds) Electrochemical and thermal modeling of battery, fuel cell and photoenergy conversion systems. (The Electrochemical Society proceedings series, vol PV 86-12) The Electrochemical Society, Pennington, NJ, p 114
91. Ruetschi P (1988) J Electrochem Soc 135: 2657
92. Mo Y, Hwang E, Scherson DA (1996) J Electrochem Soc 143: 37
93. Kim M, Kim K (1998) J Electrochem Soc 145: 507
94. Cordoba-Torresi SI, Gabrielli C, Goff AH-L, Torresi R (1991) J Electrochem Soc 138: 1548
95. Singh D (1998) J Electrochem Soc 145: 116
96. Szytula A, Murasik A, Balanda M (1971) Phys Status Solidi B 43: 121